Radiation Test Results for Semiconductor Technology Associates STA0100 and STA0120 P-channel CCDs

Heidi N. Becker and Tom Elliott
Jet Propulsion Laboratory
California Institute of Technology

November 22, 2006

NASA Electronic Parts & Packaging Program
FY06 Sensor Technology (Radiation) Task: CMOS FPAs and P-CCDs
NASA WBS: 939904.01.11.30 Task#: 06-090j
JPL Project: 102197 JPL Task #3.21.4

1.0 Introduction

This report describes the results of ionizing dose and displacement damage dose testing for two Semiconductor Technology Associates p-channel charge-coupled devices (CCDs). The study was performed in FY06 under the sponsorship of the NASA Electronic Parts and Packaging Program's continuing Sensor Technology (Radiation) Task.

1.1 Charge Transfer Efficiency Performance in P-channel CCDs

Charge transfer efficiency (CTE) degradation from non-ionizing dose (displacement damage) is a well known radiation degradation mechanism affecting buried n-channel CCDs. Degraded CTE is caused by radiation-induced defects in the silicon of the buried channel. These defects trap a fraction of the signal charge, releasing it at some time after the main charge packet has been transferred to the next pixel. This can cause a smeared signal, such as a star signal with a deferred charge tail, or a total loss of some fraction of the signal, dependent on the emission time constant of the dominant charge trap and the operational temperature and timing used for charge transfer. Much experimentation has indicated that the dominant charge trap for n-channel CCDs operated near room temperature is the phosphorous-vacancy complex, or "E-center" [1, 2]. The E-center is an electron trap with an energy level approximately 0.44 eV below the conduction band. The trap re-emission time near room temperature (on the order of a millisecond at -20C) is often unfavorable to transfer rates chosen for space applications such as star tracking.

In buried p-channel CCDs, the signal carriers are holes, not electrons, leading to the prediction [3] that the major radiation-induced trap that can degrade CTE in p-CCDs is the divacancy hole trap. This trap is shallow, with an energy level of ~0.21 eV. Near room temperature the emission time constant is only ~0.1 microseconds, so for many applications holes would be captured and re-emitted before the next charge transfer. An additional argument for this prediction is that the divacancy is formed by a second order process while the E-center is formed by a first order process [3], so for a given displacement damage dose, fewer divacancies should be formed than E-centers, which are ineffective hole traps. A process involving a modification of the doping of the buried channel, called "defect gettering" (not used in the p-CCDs studied here), can also be employed to deliberately boost the production of E-centers relative to divancacies during irradiation.

1.2 STA P-channel CCD Device Descriptions

The focal plane arrays discussed in this report are two variants of a recent Semiconductor Technology Associates p-channel CCD design. The design is geared for star tracking applications near room temperature. Multi-phase pinning (MPP) is employed to reduce surface dark current, and both variants contain high speed (1 MHz) output amplifiers. The CCDs are 3-phase, split frame transfer, buried channel devices. They were fabricated by DALSA Semiconductor using optimized starting material. Dual dielectric insulator (SiO_2/Si_3N_4) and LOCOS (localized oxidation of silicon) processing were used. Half of the wafer lot was fabricated with 8 nm SiO_2 layers, and half with 47 nm oxide layers. The devices characterized in this study all had the 47 nm SiO_2 thickness. The CCDs were made without the use of a notch (supplementary buried channel), and were fabricated on bulk silicon; there is an approximate 10 micron depletion thickness, and an approximate 680 micron collection depth.

The two variants share the same design "footprint," and the size of both chips is 12 x 23 mm. The design variations are as follows:

STA0100 (512x512 pixel imaging area):

- 21 micron pixels in both the image and storage regions
- Full well ~200,000 electrons
- a 1 MHz dual stage output amplifier at each of the four corners of the chip
- all 4 amps can be read out simultaneously
- top and bottom serial registers are both split
- 2 top quadrants must be read out at the same time
- 2 bottom quadrants must be read out at the same time
- top and bottom halves of the array may be read out at the same time or independently
- channel stop in the center of the array does not allow for 1024 x 512 or 1024 x 256 readout

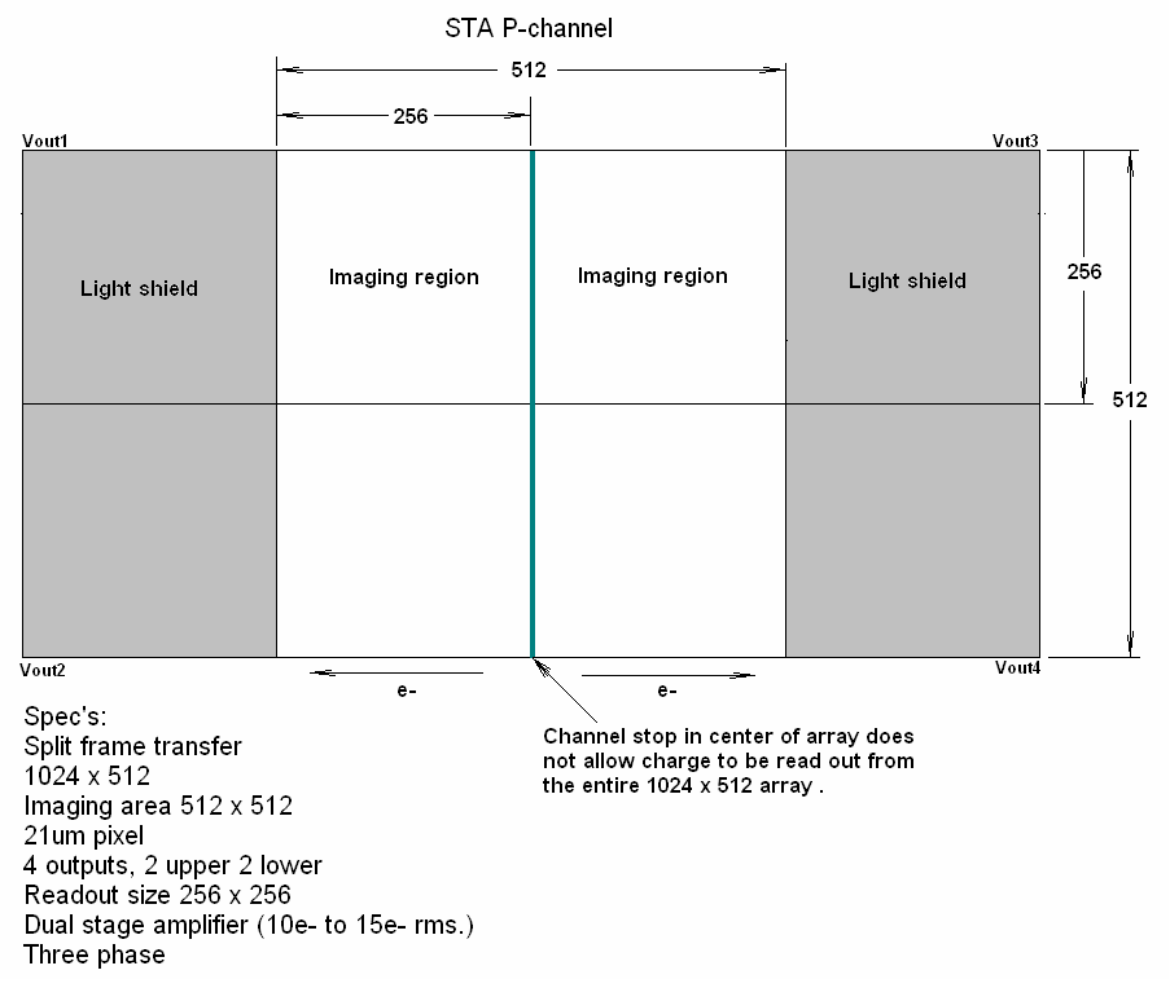

Fig. 1. STA0100 512x512 p-CCD design

STA0120 (1024x1024 pixel imaging area):

- 10.5 micron pixels in both the image and storage regions
- 16 1-MHz dual stage output amplifiers (8 upper, 8 lower)
- all 16 amps can be read out simultaneously
- all upper readouts must be read out together
- all lower readouts must be read out together
- top and bottom halves of the array may be read out at the same time or independently
- readout area size: 128 (horizontal) x 512 (vertical) pixels
- no channel stop, so a 128 x 2048 area may be read out

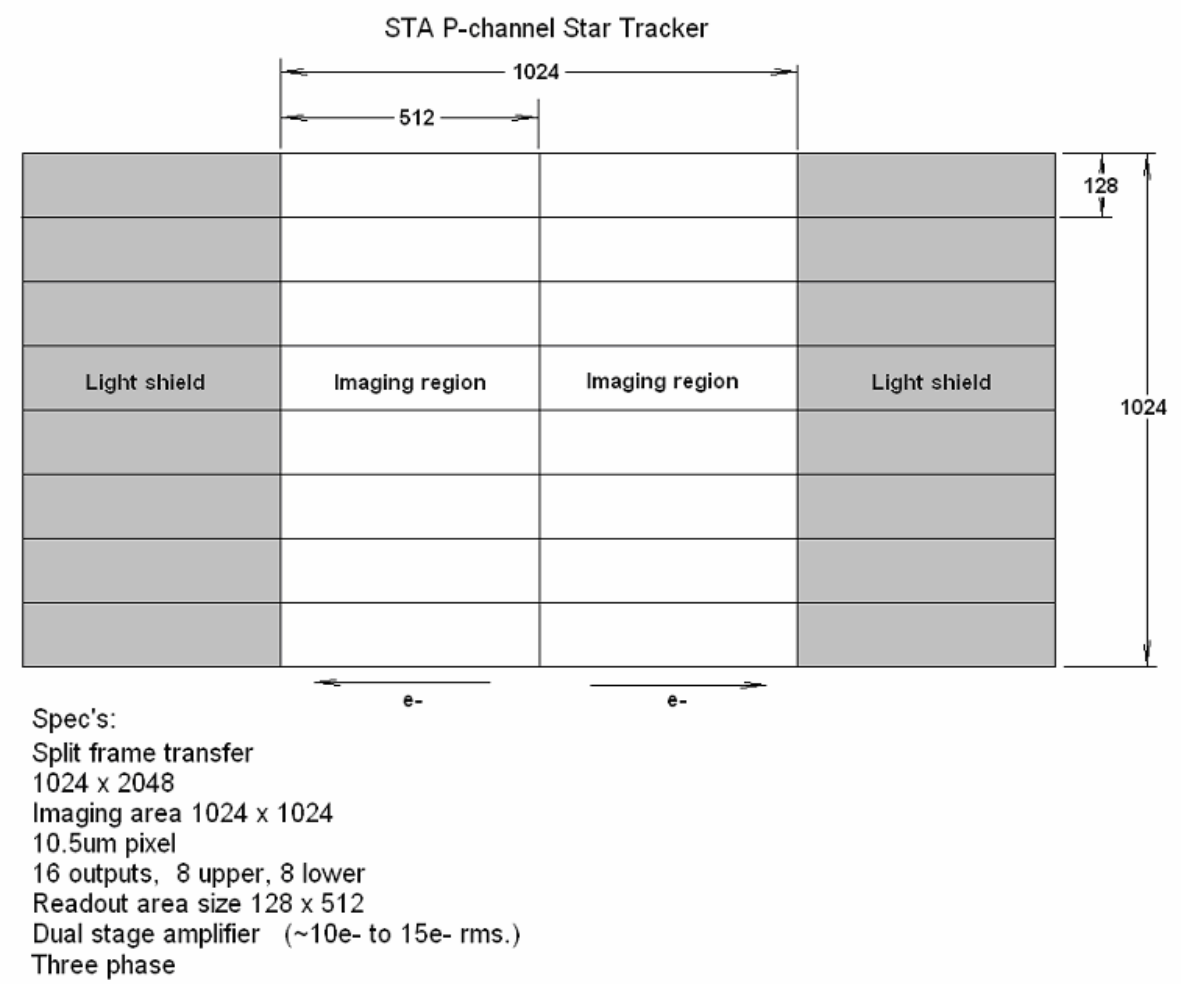

Fig. 2. STA0120 1024x1024 p-CCD design

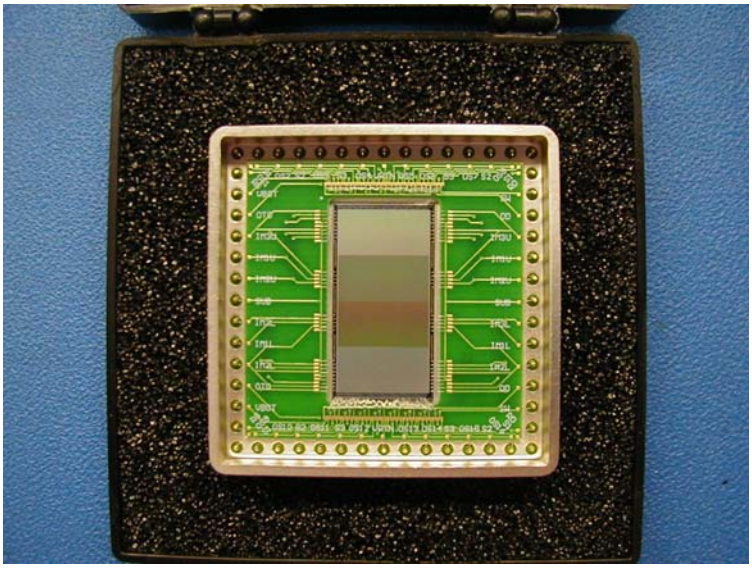

Fig. 3. The 16-output STA0120 "star tracker" p-CCD in new Kovar packaging.

The performance of the 512^2 STA0100 device was recently characterized by Spratt et. al [3] following irradiation with 40-MeV protons. In their paper, they demonstrated both excellent pre-irradiation charge transfer efficiency (CTE) and the relatively low proton-induced CTE degradation that is to be expected for p-channel CCDs compared to n-channel CCDs. Their study phase was complete prior to obtaining dark signal distribution data or performing ionizing dose testing, and the original packaging design (used in their study) made temperature control of the devices difficult. We report on hot pixel performance and unbiased ionizing dose response herein, in addition to extensive pre- and post-proton irradiation characterization of CTE (at temperatures ranging from -100C to -20C) and dark current (characterized from -40C to room temperature). These measurements were facilitated by a new windowless Kovar packaging design, implemented for this NEPP study, which allowed for improved thermal contact between the CCD package and our camera's cold finger. Our study also is the first to examine the radiation response of the STA0120 1024^2 variant.

2.0 Test Methods

2.1 63-MeV Proton Testing

Extensive pre- and post-irradiation characterization was performed on the 512^2 and 1024^2 technologies. Samples were irradiated unbiased, with all leads shorted and grounded, at ambient temperature. 63.3-MeV protons and a 1E7 p/cm^2 *s flux were used for all the proton irradiations. Table 1 shows the radiation test levels used for the four 512^2 samples and the two 1024^2 samples that were tested with protons. All six samples were taken from the same wafer, "Wafer 7."

Table 1. Proton irradiation levels used in the study.

Device Type	Sample	63-MeV fluence (p/cm^2)	Displacement Damage Dose* (MeV/g)	Total Ionizing Dose (krad(Si))
512^2	W7 D5	6.25E9	~2E7	0.84
512^2	W7 D2	1.5E10	~5E7	2.0
512^2	W7 D3	1.5E10	~5E7	2.0
512^2	W7 D6	3E10	~1E8	4.0
1024^2	W7 D9	1.5E10	~5E7	2.0
1024^2	W7 D10	3E10	~1E8	4.0

*The 40-MeV proton testing described in [3] included displacement damage dose levels ranging from 1E7 to 1E8 MeV/g, with the majority of samples irradiated to ~2E7 MeV/g. We assume a 63-MeV proton NIEL value of 3.5E-3 MeV * cm^2/g.

2.1.1 Charge Transfer Efficiency

Charge transfer efficiency was characterized at temperatures ranging from -100C to -20C, using Cd-109 hard x-rays. An x-ray fluence of approximately 40 events per line was applied during a 3-4 second integration time, using a mechanical shutter between the source and the CCD. The K_α line of Cd-109 creates a signal of ~6,300 electrons per x-ray in silicon. Following irradiation with 40-MeV protons, Spratt et al. [3] sited difficulty in using Fe-55 x-rays (~1620 electron signal) for CTE characterization near room temperature. This was due to trouble discerning the small signal in the presence of the dark current non-uniformities created by the irradiation. This result prompted us to use a larger x-ray signal. Both CCD variants were characterized using 100 kHz and 250 kHz readout rates. The readout approaches for each technology were as follows:

STA0100: A 512x512 portion of the array was read out through a single amplifier to allow the largest number of vertical and horizontal transfers and, therefore, the most optimal statistics on CTE. The presence of the channel stop in the middle of the array precluded a 1024x512 readout. We were not limited to a 256x512 readout, as would have been the case with an optical signal, because Cd-109 x-rays are able to penetrate the aluminum-coated storage regions of the STA0100.

For 100 kHz readouts, horizontal transfer time was 10 μs per pixel and ~5 ms per line. Vertical line transfer time was 5.32 ms (including an ~200 μs line shift time, and the 5.12 ms dwell time during readout of the preceding line).

For 250 kHz readouts, horizontal transfer time was 4μs per pixel and ~2 ms per line. Vertical line transfer time was 2.2 ms (including an ~100 μs line shift time, and the 2 ms dwell time during readout of the preceding line).

STA0120: A 1500x128 portion of the array (including a portion of the lower storage region) was read out through a single amplifier. While this readout approach gave very good statistics on vertical CTE, the statistics for horizontal CTE were not as optimal. However 128 pixels is the maximum achievable line size for the STA0120 due to its 16-amplifier design.

For 100 kHz readouts, horizontal transfer time was 10 μs per pixel and 1.28 ms per line. Vertical line transfer time was 1.48 ms (including a 200 μs line shift time, and the 1.28 ms dwell time during read out of the preceding line).

For 250 kHz readouts, horizontal transfer time was 4 μs per pixel, and 0.5 ms per line. Vertical line transfer time was ~0.6 ms (including a ~100 μs line shift time, and the 0.5 ms dwell time during readout of the preceding line).

2.1.2 Dark Signal

Dark signal was characterized at temperatures ranging from room temperature to -40C in approximately 7 degree increments. Two dark frames were taken at each temperature. Integration times at the different temperatures were varied so that hot pixels would not saturate the camera's ADC. The array areas used for dark current characterizations were 450 x 450 pixels for the STA0100 and 1400 x 100 for the STA0120.

2.1.3 Flat Band Shifts

The samples were also evaluated for flat band shifts and any changes to the inversion breakpoint.

2.2 Ionizing Dose Testing

512^2 samples from a different wafer had to be used for Co-60 gamma ionizing dose testing, because all available packaged samples from Wafer 7 had been spent during proton testing. Samples W6 D3 and W6 D4 were irradiated unbiased, with all leads shorted and grounded.

These samples were examined for increased dark signal, flat band shifts, and any change to the inversion breakpoint. Step-level irradiation was performed on both devices to: 4 krad(Si), 10 krad(Si) and 20 krad(Si) (cumulative). The dose rates were 2 rad(Si)/s for W6 D3 and 4 rad(Si)/s for W6 D4.

3.0 Test Results

3.1 Charge Transfer Efficiency

The following six tables list baseline (pre-irradiation) and post-irradiation CTE values for each of the six samples from Wafer 7. The results of Cd-109 CTE characterization for the four STA0100 and two STA0120 samples irradiated with 63-MeV protons are shown. For temperature conditions where table entries are blank, post-irradiation dark signal non-uniformities were large enough to prevent reliable determination of CTE.

Table 2. W7 D5 STA0100 (6.25E9 p/cm^2)

Temp. C	100Khz Baseline Horizontal W7 D5	100Khz Post Rad Horizontal W7 D5	100Khz Baseline Vertical W7 D5	100Khz Post Rad Vertical W7 D5	250 Khz Baseline Horizontal W7 D5	250Khz Post Rad Horizontal W7 D5	250Khz Baseline Vertical W7 D5	250Khz Post Rad Vertical W7 D5
-20	>.99999	>.99999	>.99999	>.99999	>.99999	>.99999	>.99999	>.99999
-30	>.99999	>.99999	>.99999	.999978	>.99999	.99997	>.99999	.999966
-40	>.99999	.99996	>.99999	.999973	>.99999	.999963	.999987	.999937
-50	.999969	.999954	.999978	.999973	.999975	.999944	.999976	.999938
-60	.999978	.999944	.999978	.999944	.999968	.999937	.999969	.999937
-70	.999969	.999945	.999967	.999926	.999969	.999944	.999963	.999932
-80	.999970	.999954	.999970	.999939	.999969	.999962	.999963	.999924
-90	.999979	.999963	.999958	.999939	.999975	.999970	.999963	.99991
-100	.999982	.999963	.999964	.999936	.999981	.999976	.999954	.99991

Table 3. W7 D2 STA0100 (1.5E10 p/cm^2)

Temp. C	100Khz Baseline Horizontal W7 D2	100Khz Post Rad Horizontal W7 D2	100Khz Baseline Vertical W7 D2	100Khz Post Rad Vertical W7 D2	250 Khz Baseline Horizontal W7 D2	250Khz Post Rad Horizontal W7 D2	250Khz Baseline Vertical W7 D2	250Khz Post Rad Vertical W7 D2
-20	>.99999		>.99999		>.99999	>.99999	>.99999	
-30	>.99999		>.99999		>.99999	.999963	>.99999	
-40	>.99999	.99999	>.99999	.999909	>.99999	.999928	.99999	.999891
-50	.999974	.99988	.999976	.999909	.999978	.999918	.999961	.999853
-60	.999984	.999837	.999969	.999889	.999969	.999923	.999961	.999864
-70	.999970??	.999826	.999967	.999879	.999970	.999924	.999955	.999881
-80	.999982	.999837	.999958	.999837	.999970	.999911	.999960	.999882
-90	.999978	.999824	.999955	.999834	.999975	.999894	.999963	.999804
-100	.999981	.999847	.999964	.999872	.999978	.999893	.999942	.999811

Table 4. W7 D3 STA0100 (1.5E10p/cm^2)

Temp. C	100Khz Baseline Horizontal W7 D3	100Khz Post Rad Horizontal W7 D3	100Khz Baseline Vertical W7 D3	100Khz Post Rad Vertical W7 D3	250 Khz Baseline Horizontal W7 D3	250Khz Post Rad Horizontal W7 D3	250Khz Baseline Vertical W7 D3	250Khz Post Rad Vertical W7 D3
-20	>.99999		>.99999		>.99999		>.99999	
-30	>.99999	.999982	>.99999	.999924	>.99999	.999942	>.99999	.999927
-40	>.99999	.999961	>.99999	.999953	.99999	.999937	>.99999	.999891
-50	.99998	.999924	.999975	.999920	.999972	.999927	.999963	.999889
-60	.999981	.999914	.999973	.999897	.999969	.999926	.999963	.999855
-70	.999981	.999890	.999970	.999845	.999972	.999909	.999955	.999837
-80	.999984	.999892	.999955	.999832	.999970	.999879	.999954	.999822
-90	.999979	.999865	.999954	.999848	.999972	.999875	.999948	.999804
-100	.999980	.999898	999969	.999845	.999979	.999893	.999947	.999815

Table 5. W7 D6 STA0100 (3E10 p/cm^2)

	100Khz	100Khz	100Khz	100Khz	250 Khz	250Khz	250Khz	250Khz
Temp. C	Baseline Horizontal W7 D6	Post Rad Horizontal W7 D6	Baseline Vertical W7 D6	Post Rad Vertical W7 D6	Baseline Horizontal W7 D6	Post Rad Horizontal W7 D6	Baseline Vertical W7 D6	Post Rad Vertical W7 D6
-20	>.99999		>.99999		>.99999		>.99999	
-30	>.99999	.999971	>.99999		>.99999	.99991	>.99999	.99988
-40	>.99999	.999908	>.99999	.99986	.99997	.99988	>.99999	.99979
-50	.99996	.99990	.99998	.99981	.999969	.99985	.999976	.99975
-60	.99998	.99984	.99998	.99979	.999963	.99987	.99997	.99973
-70	.99997	.99983	.99997	.99977	.999969	.99989	.999963	.99971
-80	.999982	.99985	.999951	.99970	.999969	.99988	.999954	.99970
-90	.999978	.99986	.999951	.99967	.999970	.99988	.999940	.99964
-100	.999976	.99986	999963	.99964	.999975	.99989	.999940	.99963

Table 6. W7 D9 STA0120 (1.5E10 p/cm^2)

	100Khz	100Khz	100Khz	100Khz	250 Khz	250Khz	250Khz	250Khz
Temp. C	Baseline Horizontal W7 D9	Post Rad Horizontal W7 D9	Baseline Vertical W7 D9	Post Rad Vertical W7 D93	Baseline Horizontal W7 D9	Post Rad Horizontal W7 D9	Baseline Vertical W7 D9	Post Rad Vertical W7 D9
-40	.999885	.999858	.999920	.999982	.999888	.999797	.999976	.999953
-50	.999833	.999793	.999978	.999963	.99990	.999785	.999975	.999923
-60	.999770	.999776	.999981	.9999482	.999818	.999707	.999954	.999908
-70	.999805	.999767	.999975	.999945	.999804	.999694	.999975	.999898
-80	.99981	.999756	.999973	.999939	.999776	.999680	.999966	.999893
-90	.999816	.999745	.999971	.999922	.999766	.999739	.999956	.999897
-100	.999850	.999733	.999976	.999919	.999747	.999704	.999968	.999912

Table 7. W7 D10 STA0120 (3E10 p/cm^2)

	100Khz	100Khz	100Khz	100Khz	250 Khz	250Khz	250Khz	250Khz
Temp. C	Baseline Horizontal W7 D10	Post Rad Horizontal W7 D10	Baseline Vertical W7 D10	Post Rad Vertical W7 D10	Baseline Horizontal W7 D10	Post Rad Horizontal W7 D10	Baseline Vertical W7 D10	Post Rad Vertical W7 D10
-40	.999956	.999883	>.99999	.999956	.999806	.999825	.999981	.999937
-50	.999933	.999879	>.99999	.999951	.999804	.999810	.999975	.999936
-60	.999917	.999871	999982	.999951	.999810	.999739	.999976	.999922
-70	.999870	.999804	.999978	.999934	.999784	.999687	.999974	.999915
-80	.999849	.999787	999971	.999929	.999797	.999644	.999979	.999911
-90	.999843	.999715	999973	.999921	.999861	.999565	.999974	.999909
-100	.999883	.999797	999976	.999909	.999855	.999552	.999973	.999906

The excellent post-irradiation vertical and horizontal CTE performance at the various characterization temperatures was evaluated with respect to the emission time constant (t_e) of the divacancy hole trap. In several instances, horizontal or vertical CTE in a given sample was observed to dip at a temperature

where the transfer time (discussed in 2.1.1) was on the order of t_e. These occurrences have been highlighted in blue in Tables 2-7. However, while there were a few irradiation and temperature conditions for which the CTE degradation in a given sample appeared to be influenced by the nearness of the transfer time to t_e (for example, during 4 μs horizontal transfers of the STA0100 at ~ -50C), this was not a dominant trend.

Since proton irradiation also causes increased dark signal rates, there may be a degree of trap satisfaction by dark signal ("fat zero"). This could skew the relative importance of the divacancy emission time constant at warmer temperatures, where thermal generation of dark signal is increased, and may partially explain the relatively higher values of horizontal CTE we observed in the STA0120 at higher temperatures. There is also the possibility that our Cd-109 signal and fluence were high enough to provide enough of a fat zero to mask any more obvious correlation between CCD timing and the emission time constant of the divacancy hole trap.

In comparing post-irradiation CTE for the two STA variants, there is a difference in performance following equal displacement damage dose. Figure 4 compares vertical CTE for the two variants using a 250 kHz readout rate and an irradiation level of 3E10 p/cm^2. Note that CTE is still relatively high at this considerable displacement damage dose of ~1E8 MeV/g.

Wafer 7 Die 6 STA0100 (21 micron)

Temp. C	Baseline Vertical W7 D6	Post Rad Vertical W7 D6
-20	>.99999	-
-30	>.99999	.99988
-40	>.99999	**.99979**
-50	.999976	**.99975**
-60	.99997	**.99973**
-70	.999963	**.99971**
-80	.999954	**.99970**
-90	.999940	**.99964**
-100	.999940	**.99963**

Wafer 7 Die 10 STA0120 (10.5 micron)

Temp. C	Baseline Vertical W7 D10	Post Rad Vertical W7 D10
-20	-	-
-30	-	-
-40	.999981	**.999937**
-50	.999975	**.999936**
-60	.999976	**.999922**
-70	.999974	**.999915**
-80	.999979	**.999911**
-90	.999974	**.999909**
-100	.999973	**.999906**

Fig. 4. Vertical CTE following irradiation to 1E8 MeV/g. The two STA variants are compared.

The smaller pixel pitch of the STA0120 (10.5 micron) compared to the STA0100 (21 micron) may be the major contributor to its relatively higher post-irradiation vertical CTE. The smaller active volume would be expected to contain a proportionately smaller number of radiation induced divacancy hole traps to be encountered during each vertical transfer. Figure 5 plots the increases in charge transfer inefficiency (CTI= 1-CTE) for the 21 micron and 10.5 micron pixel technologies. The values were calculated using the CTE data presented in Fig. 4 for W7D6 and W7D10. The typical radiation-induced degradation ratio

showed about a 4.5 times greater increase in CTI for the larger pixel technology, consistent with its 4 times larger active area. The slightly higher damage ratio at some temperatures may be due to small differences in Cd-109 x-ray fluence or the exact CCD temperatures that were reached during the various characterization steps.

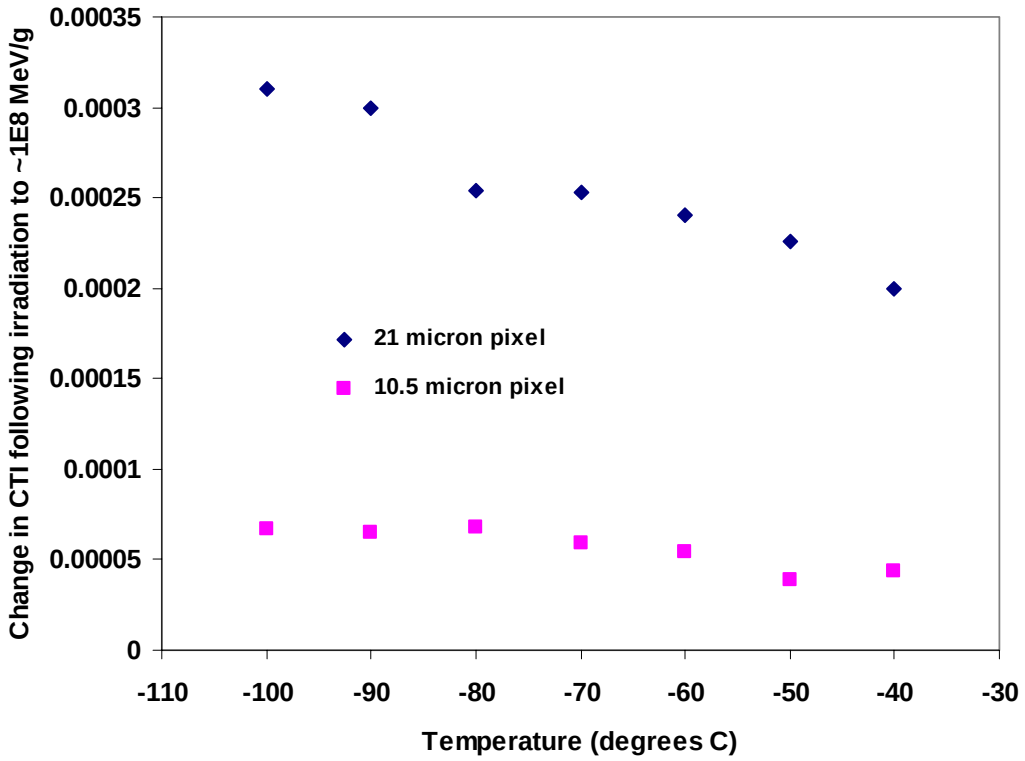

Fig. 5 The radiation-induced change in vertical CTI for the 21 micron and 10.5 micron pixel variants. This data was taken from samples that were irradiated to ~1E8 MeV/g and characterized using a 250 kHz readout. CTE degradation is approximately a factor of four higher in the 21 micron pixel variant.

As discussed by Spratt in [3], there is an open question as to whether it is 1) the second order formation of the divacancy hole trap or 2) the more favorable emission time constants of the divacancy hole trap (for many applications) that drives the good post-irradiation CTE performance in p-CCDs. It is possible that CTE degradation in these devices could show a stronger correlation between divacancy t_e and transfer time for faster readout rates than those used in this study. JPL test bed limitations restricted the maximum readout rate to 250 kHz, which is considerably slower than the 1 MHz speed at which the STA CCDs were designed to operate.

3.2 Mean Dark Signal

Proton-induced increases in mean dark signal are illustrated in the following figures. While more technically correct to express dark signal in holes/pixel*s for p-channel CCDs, we use the more familiar convention of electrons/pixel*s. The pre- and post-irradiation dark current figures of merit are also shown on the right-hand ordinates.

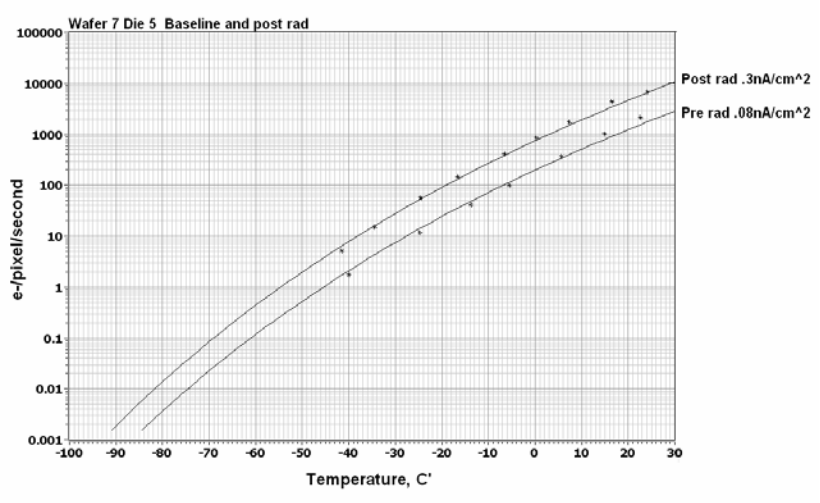

6.25E9 p/cm^2 (840 rad(Si))

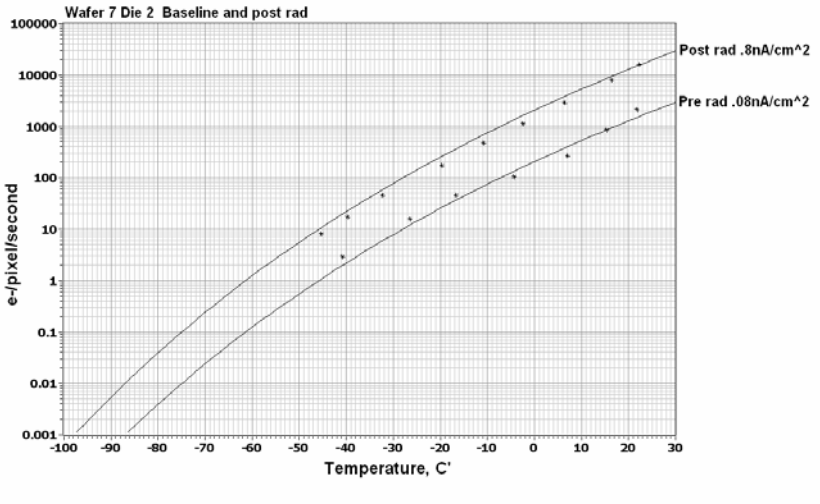

1.5E10 p/cm^2 (2 krad(Si))

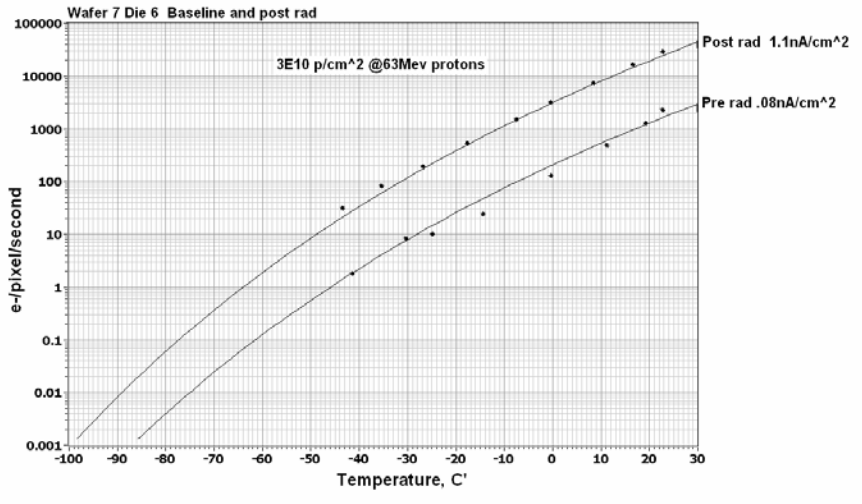

3E10 p/cm^2 (4 krad(Si))

Fig. 6. 63-MeV proton-induced increases in mean dark signal for the STA0100. Note: performance was similar for W7D2 and W7D3; W7D2 is used in this figure to represent behavior following irradiation to 1.5E10 p/cm^2.

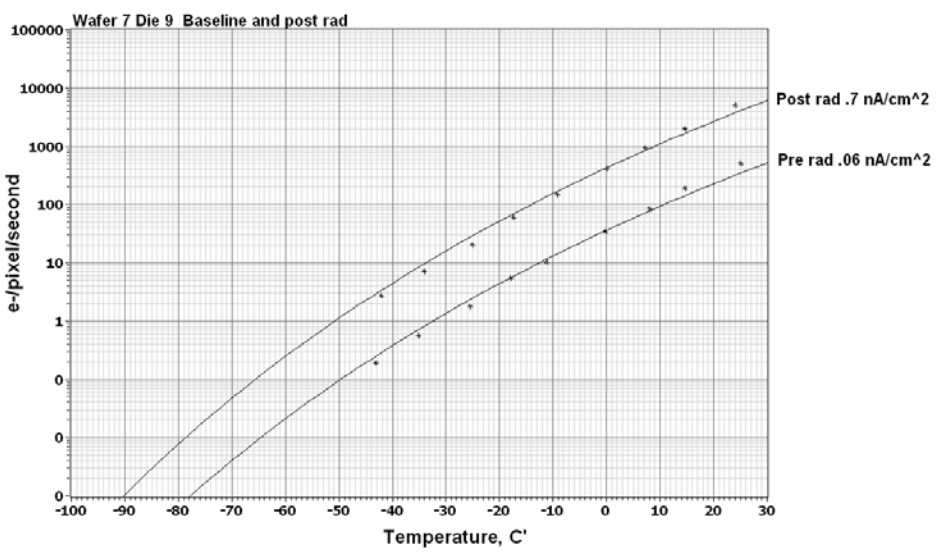

1.5E10 p/cm^2 (2 krad(Si))

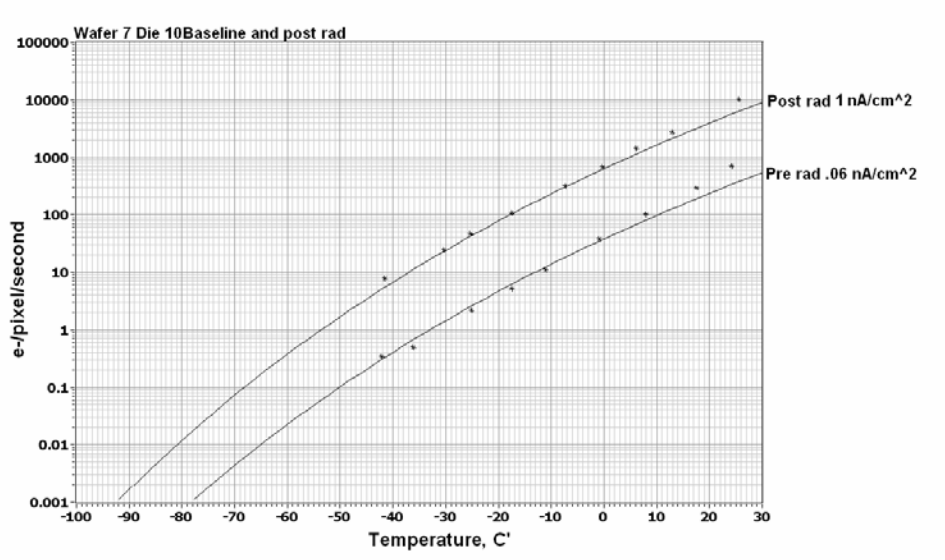

3E10 p/cm^2 (4 krad(Si))

Fig. 7. 63-MeV proton-induced increases in mean dark signal for the STA0120.

Mean dark signal increased linearly with displacement damage dose, and the rate of increase was observed to be approximately 4 times larger for the STA0100 than the STA0120. This was not unexpected, given the corresponding factor of 4 difference in pixel pitch, and the known dependence of displacement damage induced dark current on active volume. Figure 8 compares DDD-induced changes in dark signal at room temperature for the two STA variants. The rates of increase were ~1E-8 nA/cm^2 per MeV/g for the STA0100 and ~2.5E-9 nA/cm^2 per MeV/g for the STA0120. Our rate of increase for the STA0100 was of the same order as that observed in [3], but our pre-irradiation dark signal values are over an order of magnitude *less*. The radiation study described in [3] utilized the 8 nm oxide version of the STA0100, but this would not easily explain the observed differences in dark signal. It may be that we operated the STA0100 in a more fully inverted mode than that used in [3].

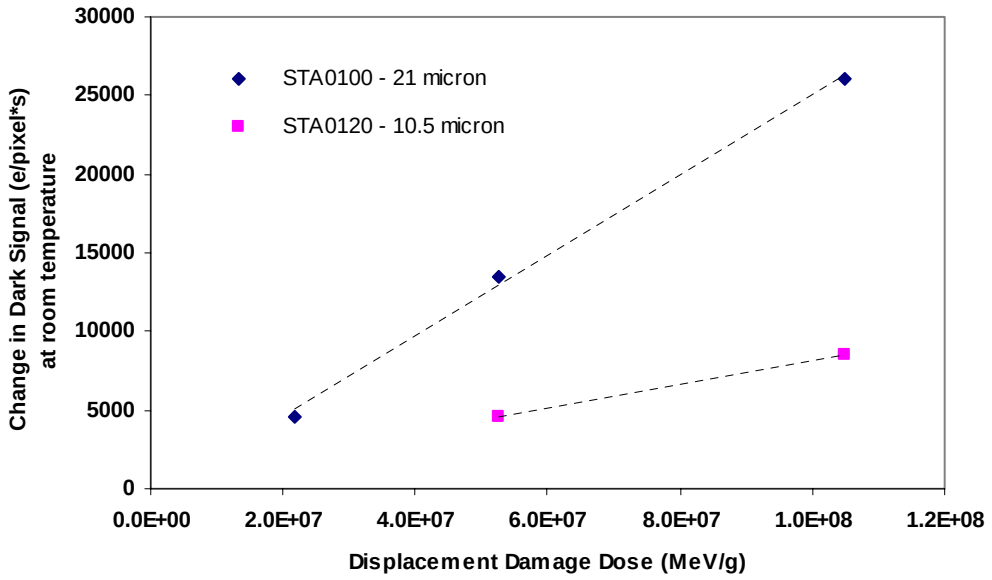

Fig. 8. Changes in dark signal (@ room temperature) vs. DDD for the STA0100 and STA0120.

Separate unbiased irradiation of the STA0100 with Co-60 suggests that ionizing dose is a relatively small contributor to mean dark signal increases from protons. Figure 9 shows changes in dark signal at room temperature as a function of ionizing dose (unbiased Co-60 sample W6D3). At the 4 krad(Si) level, the increase in dark signal was ~1000 electrons/pixel*s at room temperature. This is ~26 times less than the increase seen in the STA0100 sample that was irradiated with protons to 3E10 p/cm^2 (4 krad(Si)).

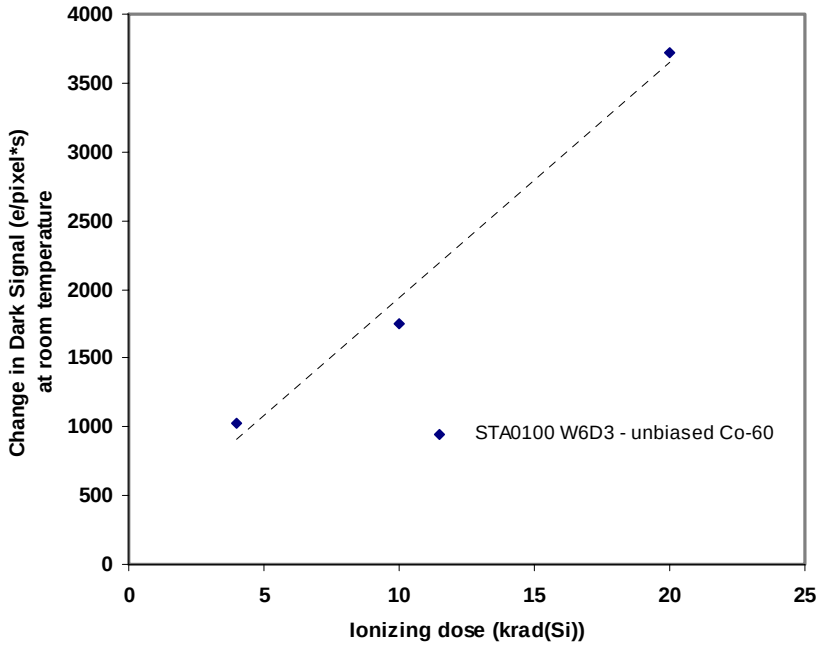

Fig. 9. Changes in dark signal (@ room temperature) vs. TID for the STA0100.

3.3 Dark Signal Non-Uniformities

The following figures show dark signal distributions for each of our samples irradiated with protons. For each sample, pre- and post-irradiation histograms are shown together for data collected at ~0-7C. The irradiation level and the post-irradiation mean dark signal level (and sigma) are also shown for each sample. The impact of pixel pitch can again be seen in the post-irradiation dark signal distributions for a given DDD. In particular, compare W7D6 (STA0100 @ 3E10 p/cm^2) to W7D10 (STA0120 @ 3E10 p/cm^2).

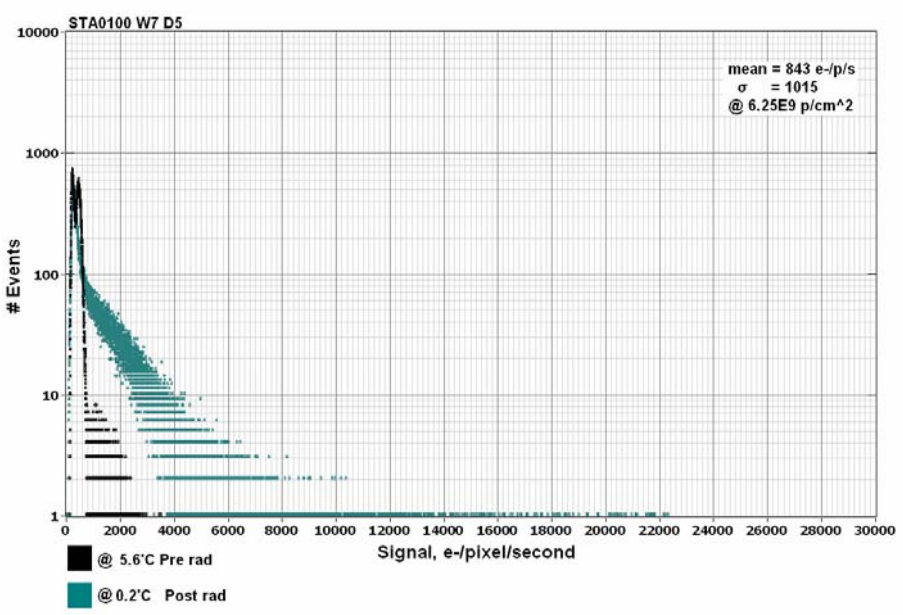

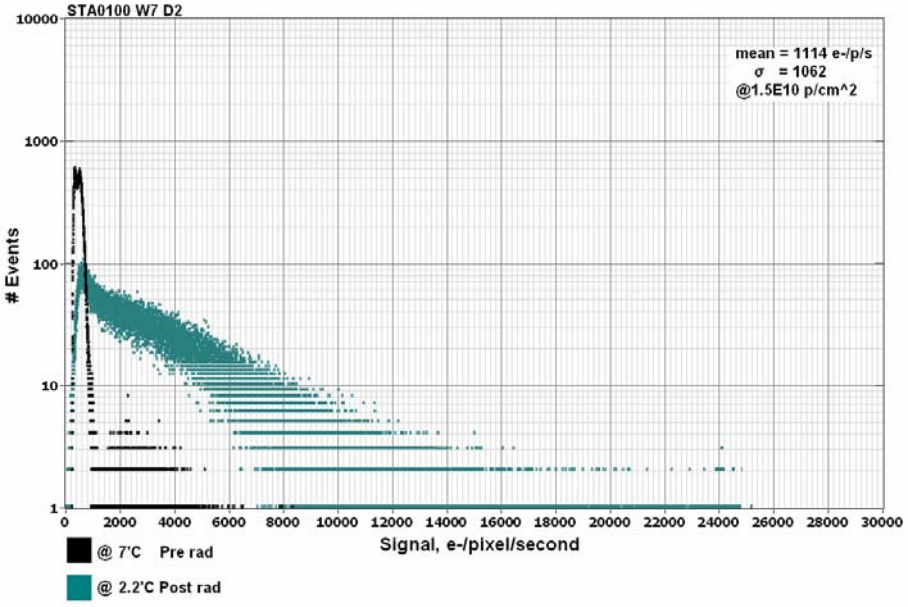

Figures continued on page 16

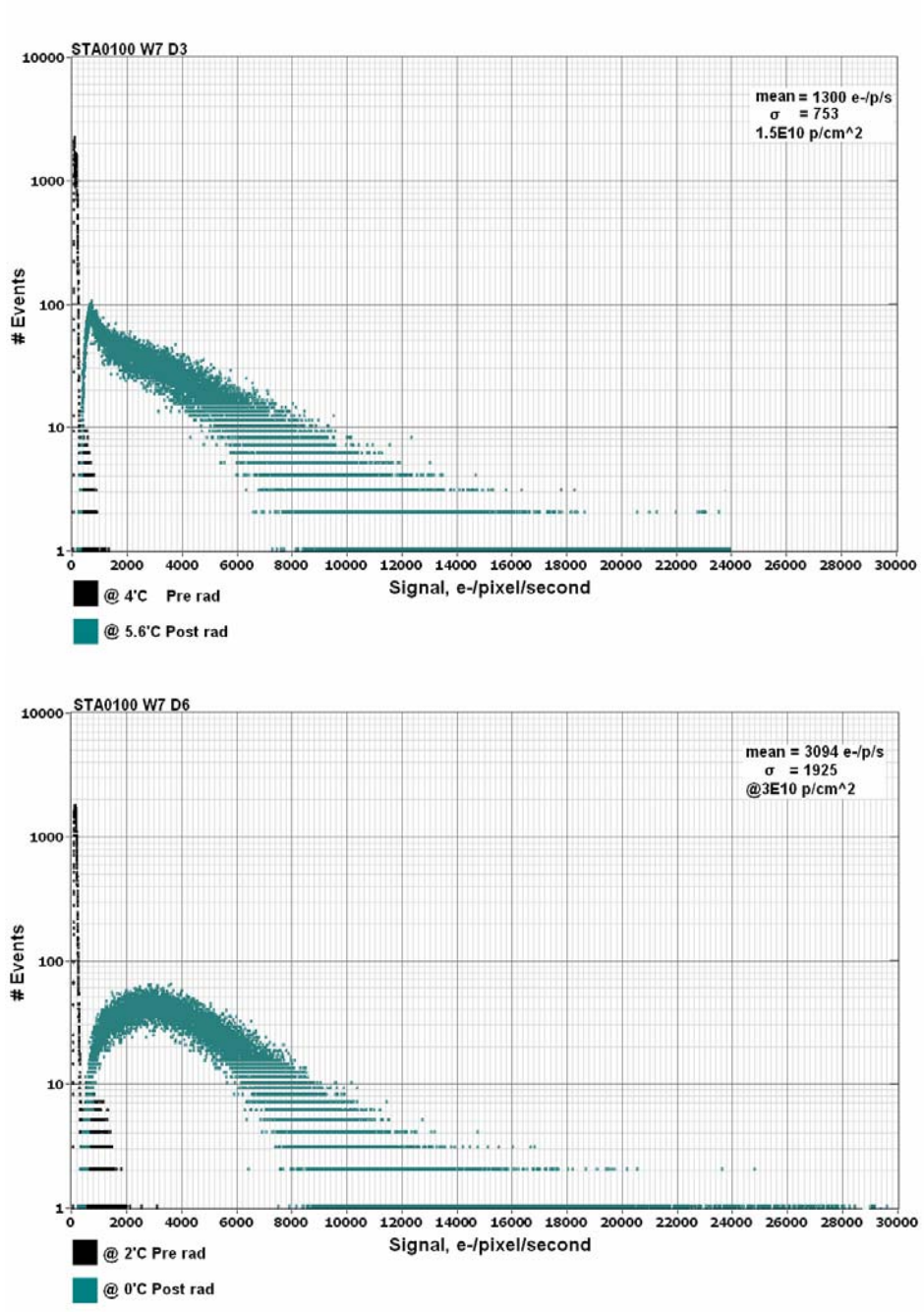

Fig. 10. Pre- and post irradiation dark signal distributions for STA0100 samples irradiated with 63-MeV protons.

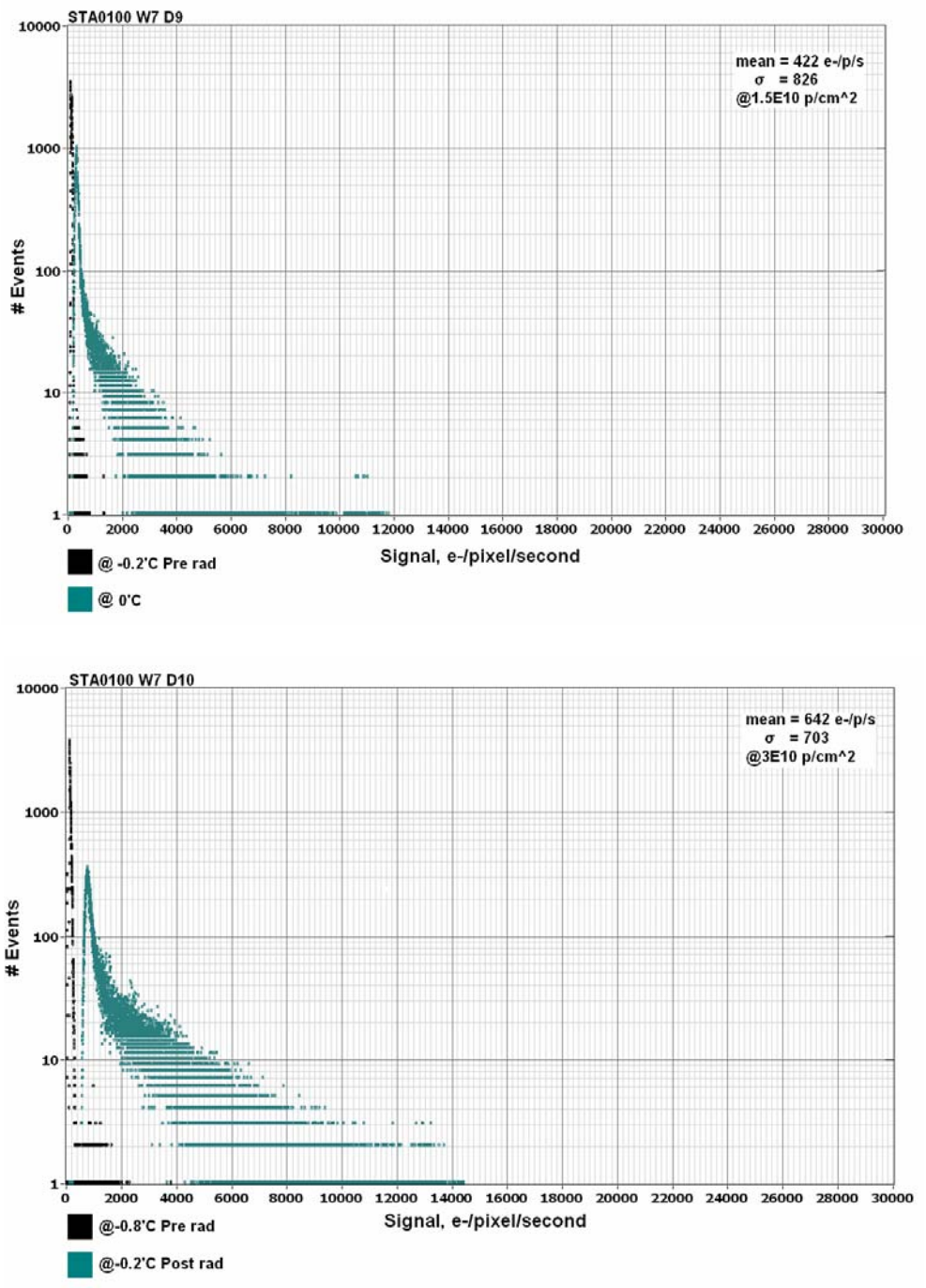

Fig. 11. Pre- and post irradiation dark signal distributions for STA0120 samples irradiated with 63-MeV protons.

The “hotter” pixels in the distributions showed reduced activation energies, compared to pixels with dark signal rates near the mean (the mean value was 0.60 to 0.65 eV, depending on the sample). This has been seen previously in both n- and p-channel CCDs [4], and is attributed to field enhanced emission. Figure 12 shows some representative activation energies and corresponding dark signal rates (at 0C) for hot pixels in STA0100 sample W7D5.

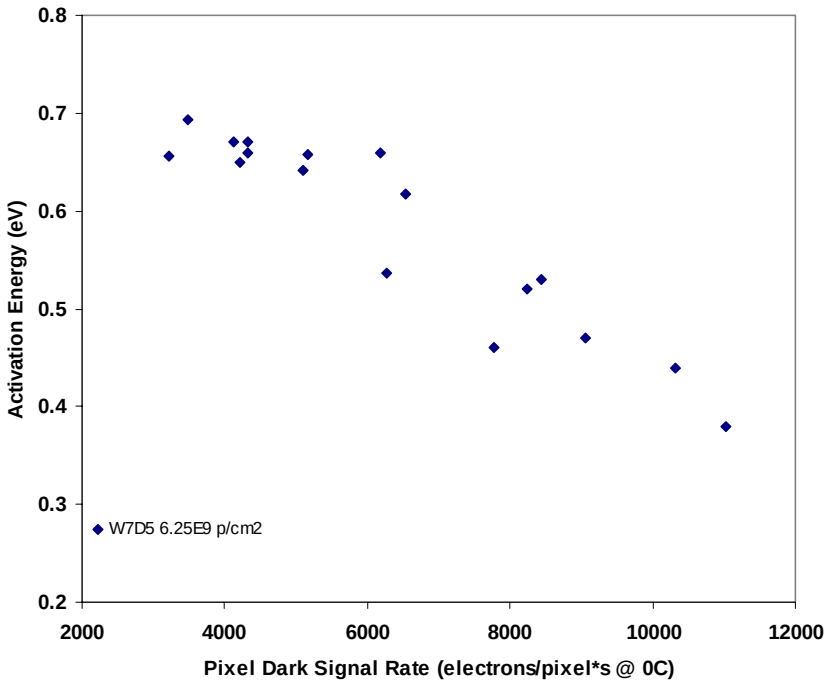

Fig. 12. Activation energies for a sampling of hot pixels in STA0100 sample W7D5 (following irradiation to 6.25E9 p/cm^2).

The following sets of figures show changes in the dark signal distributions for STA0100 sample W7D5 as the device temperature is reduced from approximately room temperature to -40C.

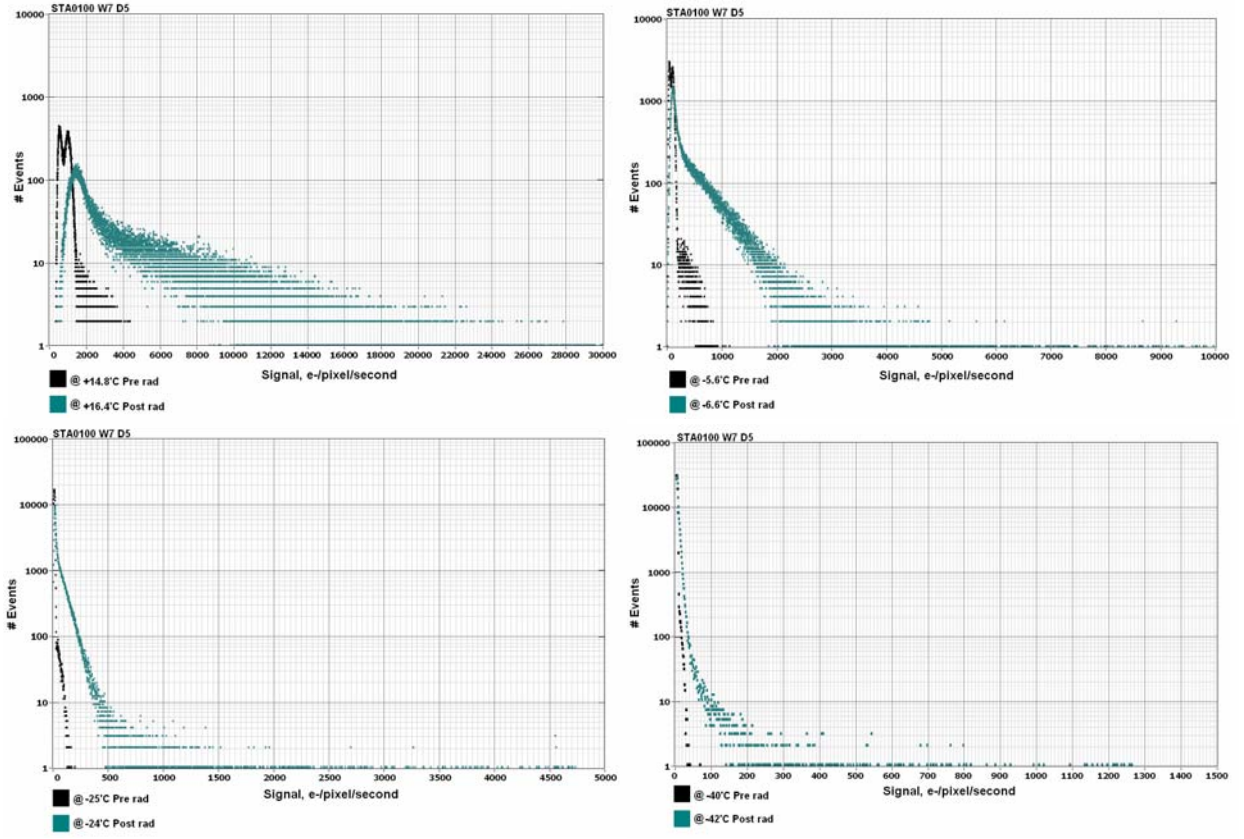

Fig. 13. Dark signal distributions in STA0100 sample W7D5 at various temperatures ranging from approximately room temperature to -40C.

Pre- and post-irradiation dark signal distributions for unbiased Co-60 sample W6 D3 are shown in Fig. 14. Note that the post-irradiation tails to the distributions are much less pronounced for the Co-60 sample than they were in the proton samples. This is due to the relatively smaller production of hot pixels following gamma irradiation, which imparts minimal DDD. The two peaks in the baseline and 4 krad(Si) distributions represent slightly different average dark signal rates in the imaging and storage regions of the array. Prior to irradiation, and after 4 krad(Si), the average dark signal rate was higher in the imaging area of the array. At 10 krad(Si) the dual peaks begin to converge, and at 20 krad(Si), the situation has shifted such that the higher peak in the distribution is for the storage region. Other experimentalists have also observed higher TID-induced dark signal increases in regions of the array that contain metallization, such as aluminum-coated storage regions [2].

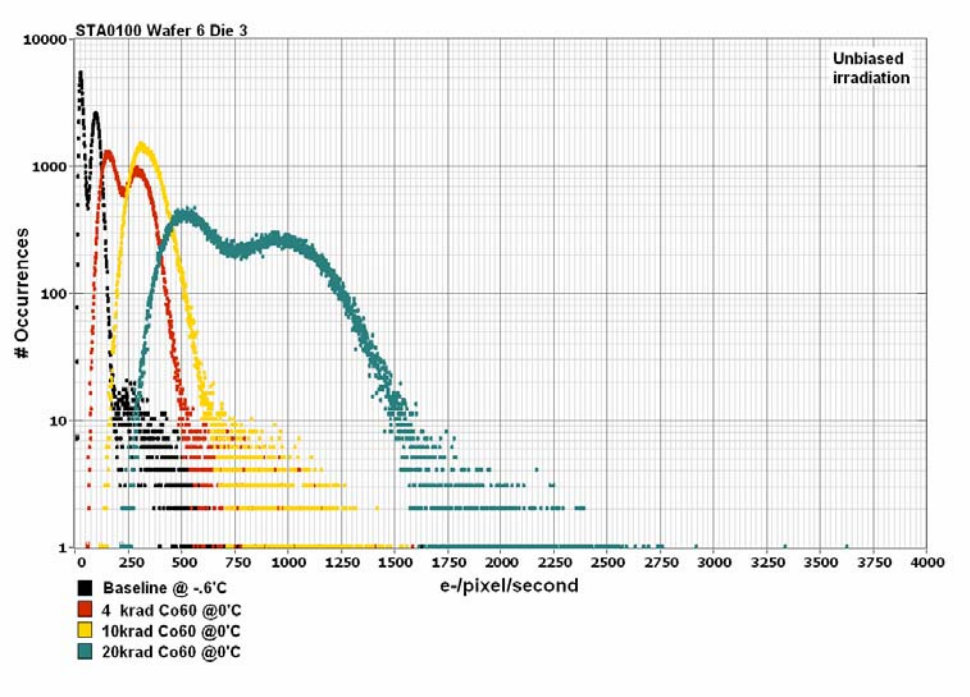

Fig. 14. Dark signal distributions for unbiased Co-60 sample W6D3.

3.4 Flat Band Shifts

Flat band shifts following proton irradiation were comparable to those typically seen for unbiased CCD irradiations (~0.05 to 0.1V per krad(Si)). None of the proton samples exhibited post-irradiation shifts in their inversion breakpoint.

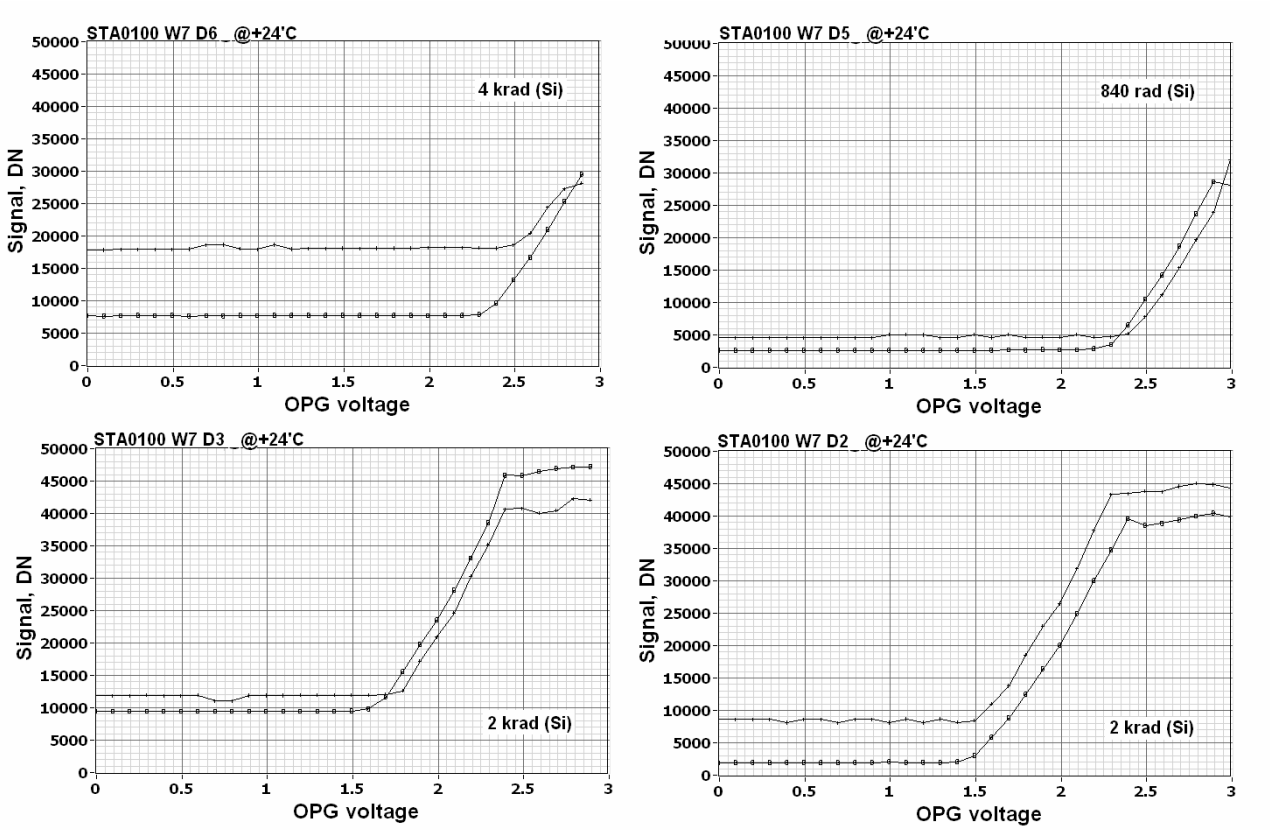

Fig. 15. Output gate flat band shifts in the STA0100 following unbiased proton irradiation. Total ionizing dose levels are noted for each sample.

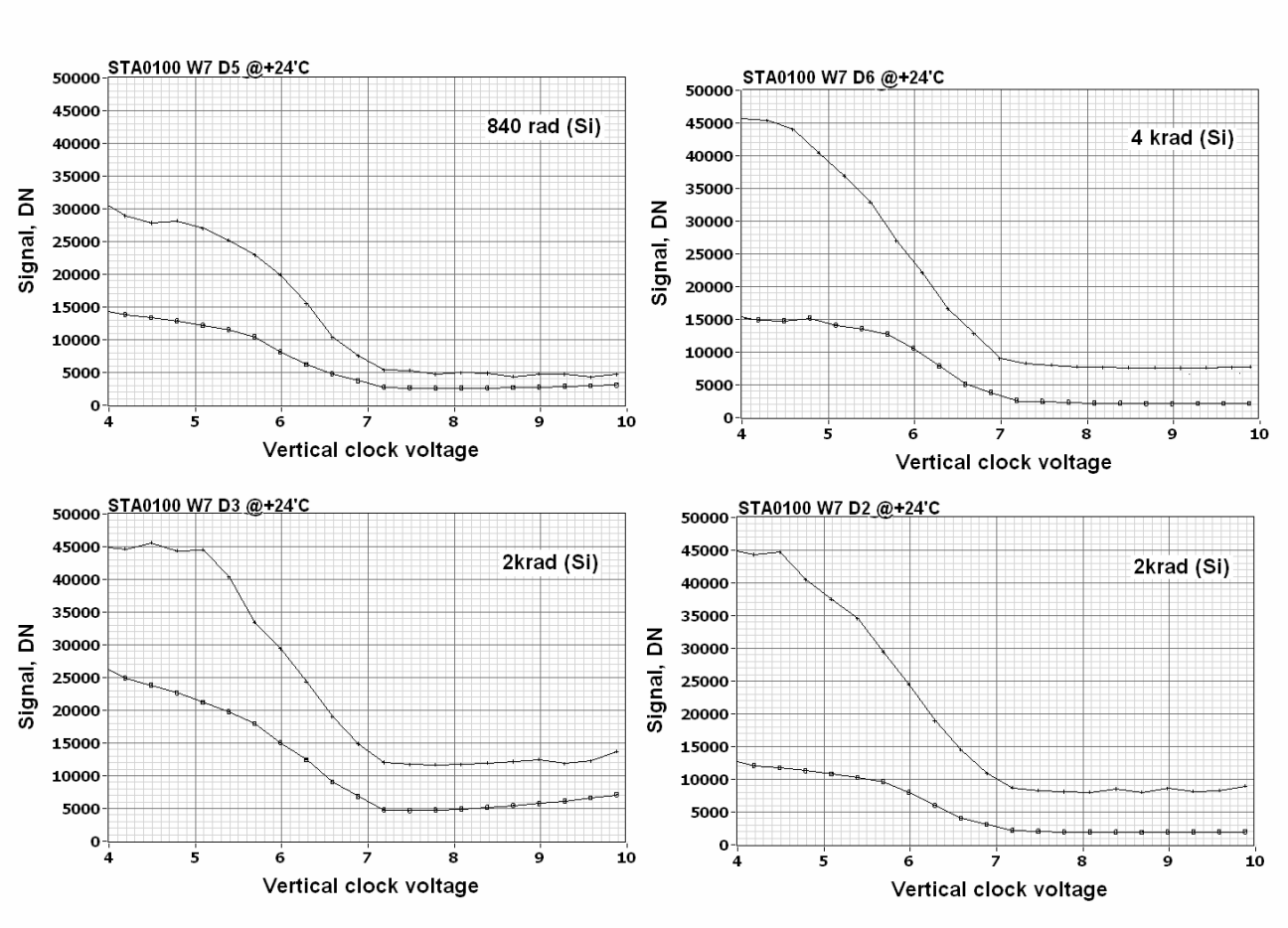

Fig. 16. Pre- and post-proton irradiation characterization of the STA0100 inversion breakpoint. STA0120 performance was similar.

The unbiased STA0100 Co-60 samples were evaluated for shifts in the inversion breakpoint at 4, 10 and 20 krad(Si). No shift was observed at 4 krad(Si) which is consistent with the unbiased proton irradiation results. However, at 10 krad(Si), an approximate 2V shift in the break point was observed (as can be seen in Fig. 17, the breakpoint was much less sharp after 10 krad(Si)). The break point remained the same following a cumulative dose of 20 krad(Si), although higher dark signal was observed than at 10 krad(Si). Shifts in VDD are illustrated in Fig. 18.

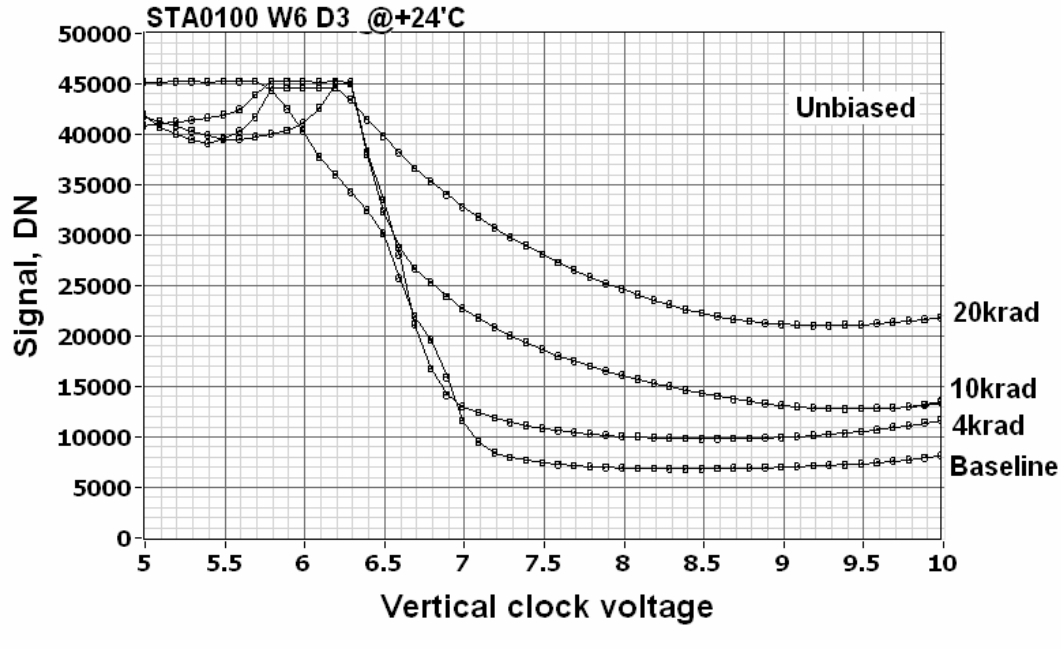

Fig. 17. Characterization of the STA0100 inversion breakpoint following unbiased irradiation with Co-60 gammas.

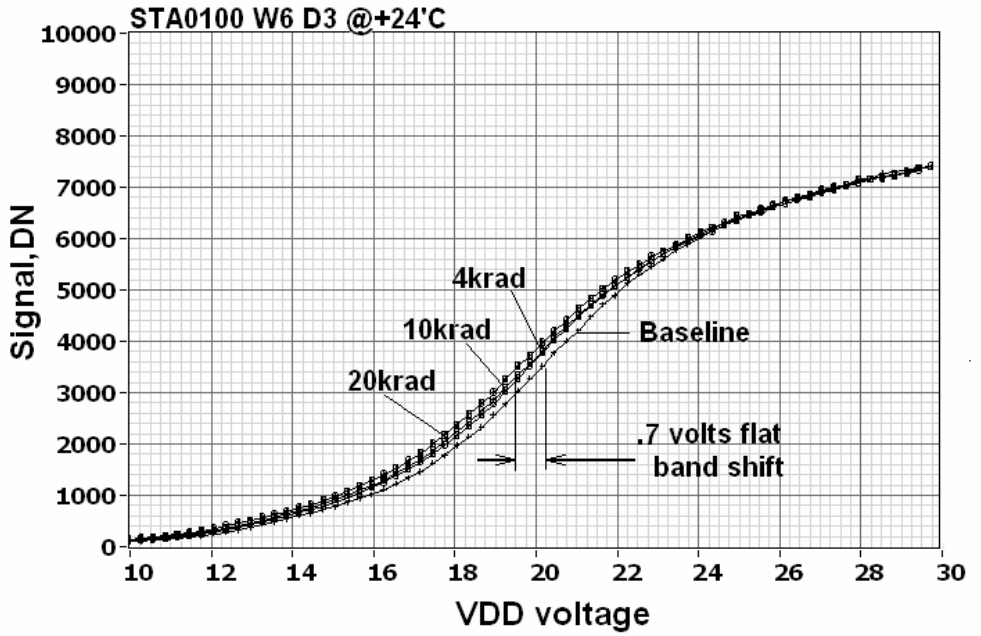

Fig. 18. Output drain flat band shifts following unbiased irradiation of the STA0100 with Co-60 gammas.

4.0 Summary & Suggestions for Further Testing

Excellent pre- and post-irradiation charge transfer efficiency was observed in these STA p-channel CCDs. We observed smaller pre-irradiation dark signal, and smaller increases in proton-induced mean dark signal than those observed in [3]. This may be because we operated our test samples in a more fully inverted mode. We have presented the first characterization of hot pixel distributions and ionizing dose performance for these CCDs.

The fabrication of these p-CCDs on bulk silicon is expected to make them particularly vulnerable to transient effects ("false signals" or a general increased background) in a solar flare or trapped particle environment. This could be mitigated by the use of epitaxial silicon (and/or thinning) in device fabrication, but such material is relatively difficult and expensive to acquire for p-CCDs. The potential high speed operation of the STA0100 and STA0120 (1-MHz) could provide a certain degree of transient mitigation dependent on the incident particle flux. Transient characterization of these devices would be an interesting follow on test, particularly from the perspective of high speed operation with windowing. There is an issue with charge diffusion in these CCDs, as was evident during CTE characterization with Cd-109. The Cd-109 x-ray signals were observed to spread between pixels, often with a single hit affecting as many as three adjacent pixels.

It would also be interesting to explore the low temperature annealing characteristics of a high performance p-channel CCD such as these. Several studies of low temperature n-channel CCD irradiations have shown significant annealing of dark signal following room temperature cycling [5, 6]. Short term annealing of mean dark signal in an n-channel CCD irradiated at -85C with 2-MeV electrons [6] was found to follow a complex process that did not obey first order kinetics. Bulk p-type silicon *has* been seen to obey first order annealing kinetics [7] after low temperature electron irradiation, so there may indeed be different low temperature irradiation characteristics between n-channel and p-channel CCDs.

5.0 Acknowledgements

We would like to thank Major Anne Clark, formerly of the Defense Threat Reduction Agency, for supplying the p-CCD wafers to the NASA Electronic Parts and Packaging Program. P-CCD packaging for this study was sponsored by the Defense Threat Reduction Agency and executed by Semiconductor Technology Associates. This research was carried out at the Jet Propulsion Laboratory, California Institute of Technology, under a contract with the National Aeronautics and Space Administration as part of the **NASA Electronic Parts and Packaging Program**. Reference herein to any specific commercial product, process, or service by trade name, trademark, manufacturer, or otherwise, does not constitute or imply its endorsement by the United States Government or the Jet Propulsion Laboratory, California Institute of Technology.

6.0 References

[1] G.R. Hopkinson, C.J. Dale, and P.W. Marshall, "Proton effects in charge-coupled devices," *IEEE Trans. Nucl. Sci.*, vol. 43, no. 2, pp. 614-627, April 1996.

[2] J.C. Pickel, A.H. Kalma, G.R. Hopkinson, and C.J. Marshall, "Radiation effects on photonic imagers – a historical perspective," *IEEE Trans. Nucl. Sci.*, vol. 50, no. 3, pp. 671-688, June 2003.

[3] J.P. Spratt, et al., "Proton damage effects in high performance p-channel CCDs," *IEEE Trans. Nucl. Sci.*, vol. 53, no. 2, pp. 423-430, April 2006.

[4] G.R. Hopkinson, "Proton damage effects on p-channel CCDs," *IEEE Trans. Nucl. Sci.*, vol. 46, no. 6, pp. 1790-1796, Dec. 1999.

[5] C.J. Marshall, et al., "Hot pixel annealing behavior in CCDs irradiated at -84ºC," *IEEE Trans. Nucl. Sci.*, vol. 52, no. 6, pp. 2672-2677, Dec. 2005.

[6] H.N. Becker, T. Elliott, and J.W. Alexander, "Electron-Induced Displacement Damage Effects in CCDs," *IEEE Trans. Nucl. Sci.*, vol. 53, no. 6, to be published in Dec. 2006.

[7] J.R. Srour, "Short-term annealing in electron-irradiated p-type silicon," *IEEE Trans. Nucl. Sci.*, vol. 17, no. 6, pp. 118-122, Dec. 1970.